Paper ID ILASS08-13-8

ANALYSIS OF DROPLET WALL INTERACTION
WITH GRADED SURFACE ROUGHNESSES

A. Müller*, K. Dullenkopf and H.-J. Bauer

Institute of Thermal Turbomachinery (ITS)
Universität Karlsruhe
Karlsruhe, Germany
* Corresponding author: armin.mueller@its.uni-karlsruhe.de

ABSTRACT
Surface properties play a significant role in droplet-wall-interaction phenomena. To enable detailed experiments considering the effect of surface roughness, two different methods for the manufacturing of wall elements with a graded surface roughness depth and width were developed. A calibrated etching method and a calibrated sandblasting method are employed. Two complete sets of wall elements with roughness depths in the range of 0 µm to 100 µm and different roughness widths in the range of 83.8 µm to 203 µm were manufactured. As primary droplets, a droplet chain with droplet diameters in the range from 40 µm to 200 µm was used. Visualization and particle tracking velocimetry (PTV) are used as diagnostic techniques. Experiments showed that both surface parameters had an influence on secondary droplet diameter, secondary droplet velocity, spray cone angle and morphology of the wall film. Furthermore, the heat transfer from the surface to the wall film is affected by roughness, too. The observed results can be explained by a thin vapour layer underneath the wall film damping primary droplet impact and affecting the heat transfer from the wall to the film.

INTRODUCION

The further development of internal combustion engines is aimed at gaining higher efficiency and emitting less pollutants. To achieve this goal, there is a general trend to higher injection pressures for fuel preparation which leads to the generation of smaller droplets in a range below 50 µm. In DISI engines, particular for stratified charge operation, spray wall interaction is an important phenomenon in the fuel distribution process. Modern injectors are characterized by high inertial velocities and small droplets. In addition to first-order factors like droplet properties and air flow, the properties of the wall enhance the level of complexity. So far, in literature experiments were performed either for smooth walls or rough walls of a fixed surface roughness. Authors in other citations vary the contact angle as well. However, in most of the known studies, no systematic investigation of the influence of the surface roughness has been conducted for the conditions of a DI engine. Comprehensive experiments were performed at the Institut für Thermische Strömungsmaschinen (ITS) since several years to fill this gap [1, 2, 3, 4, 5]. In this paper, the influence of surface roughness on droplet-wall-interaction will be examined.

Usually, droplet-wall-interaction is studied using smooth surfaces. This reduces complexity and makes modelling feasible [6]. When roughness is taken into account, there are two shortcomings: When a fixed surface roughness is used, there are too few data points for modelling. When millimeter sized droplets are used, the length scale of roughness size and droplet size is differing. Ideally, different grades of roughness are used and the droplet size is in the same magnitude as the size of the roughness elements.

There exist several models that account for surface roughness. Cossali et al. [7] give a good overview. Most prominent are the Bai-Gosman model and the Mundo Model.

Bai and Gosman [8] introduced the "Relative wall surface roughness" r_s/d_l as a correction for roughness effects. In their splashing model, they introduce a coefficient A which is depending on surface roughness r_s. This coefficient corrects for the splashing boundary. Actual measurement data is taken from Stow and Hadfield [9] where five different targets with different values of R_a in the range of 0 µm to 12 µm were used. Some typical values of A are given, but the data points are sparse, and the droplets are millimeter sized, so the correlation is not convincing. When validating the model, they see a reasonable agreement between prediction and experiments. Furthermore, they state that deviation of the roughness Δr_s, and the mean cycle of roughness L_s should be included somehow.

Similarly, Mundo et al. [10] performed experiments with one smooth surface ($R_t = 2.8$ µm) and one rough surface ($R_t = 78$µm), where R_t denotes the mean roughness height. They used initial droplets in the range 60 µm < d_0 < 150 µm, so roughness height was within that range. Surface roughness is made dimensionless in the form $S_t = R_t / d_0$. The results show, for example, that impact is more irregular and a well-defined corona is no longer identifiable. Roughness influences strongly the direction of the droplet motion, since it dissipates the tangential momentum. Also, the diameter distribution of the secondary droplets becomes narrower with a smaller mean diameter. Furthermore, there is a difference when hitting the "windward" side of a roughness element or the "leeward" side. From the data, a model for boundary between deposition and splashing is created.

Yarin and Weiss [11] performed comprehensive experiments under atmospheric conditions with droplet chains in the diameter range from 70 µm to 340 µm. The mean roughness of their surface specimen was $R_z \approx 1$ µm and 16 µm, respectively. They derived a splashing threshold correlation that also incorporates the surface roughness. In that case, roughness was much smaller than the primary droplet diameter ($R_z << D_b$), so the correlation depends only slightly on roughness.

In this paper, two complete sets of wall elements with roughness depths in the range of $R_z = 0$ µm to 100 µm and different roughness widths are examined. The primary droplets have diameters in the range from $D_b = 40$ µm to 200 µm. So, roughness element size is in the same length scale as primary droplets size.

It is well know in literature that the physical properties of the surface during droplet-wall-interaction have a considerable influence. Therefore, solid properties like specific heat capacity c_p, solid density ρ, thermal conductivity λ and contact angle are held constant at realistic values.

EXPERIMENTAL SETUP

The experimental setup consists of three main components (Figure 1): A droplet chain generator producing an equidistant chain of monodisperse primary droplets that serve as an abstraction for a DISI spray; a pressure vessel to perform measurements at the pressure level as in a cylinder during injection; and a heated wall element as analogy for the piston head where the spray is impinging most likely in the real engine.

Droplet chain generator

The vibrating orifice droplet chain generator is supported at the upper cover of the pressure vessel. This type of droplet generator proved to be the only one that is able to work under an elevated pressure of up to $p = 10$ bar (g). Driven by a pressure difference a round liquid jet exits a small orifice [12]. This jet is excited by a piezo-ceramic oscillator to form dilational waves and is split into equally sized and spaced droplets according to the Rayleigh mechanism [13]. Different orifices with round holes in the range of $d = 25$ µm to 150 µm were used, yielding droplet diameters between $D_b = 50$ µm and 300 µm. The pressure drop over the orifice controls the droplet velocity which lies between $u_b = 6$ and 22 m/s:

$$u_b = \sqrt{\frac{2 \cdot \Delta p}{\rho \cdot (1 + c_D)}} \qquad (1)$$

The mass flow rate $\dot{m}$ is directly coupled to the orifice diameter d and the primary droplet velocity u_b:

$$\dot{m}_b = \pi / 4 \cdot d^2 \cdot \rho \cdot u_b \qquad (2)$$

Depending on the operating point, the droplet frequency can be adjusted in the range of $f = 20...90$ kHz to fine-tune the droplet diameter D_b:

$$D_b = \sqrt[3]{\frac{3}{2} \frac{d^2 \cdot u_b}{f}} \qquad (3)$$

It has to be noted that for this type of droplet chain generator only two out of the four relevant parameters D_b, u_b, $\dot{m}$ and f are free parameters and the other two are dependent. In addition, orifices below $d = 30$ µm are susceptible to clogging. Therefore, most of the experiments were performed using larger orifices.

Isooctane was used as a surrogate for gasoline in all experiments. It has well defined physical properties and is less harmful than real fuel. The liquid properties of isooctane are contrasted with those of gasoline in Table 1.

Liquid	T_{sat}	Density	Surface Tension	Dynamic Viscosity
	[K]	[kg/m³]	[mN/m]	[µPa s]
Isooctane	372.4	688.8	18.2	466
Gasoline	273-483	700-740	23.0	399

Table 1. Liquid properties of isooctane and gasoline

Pressure vessel

The pressure vessel contains the heated target and is filled with an inert gas. The pressure can be adjusted up to $p = 10$ bar (g). A special window layout permits access for different optical measurement techniques, including backlight imaging, PIV and PDA.
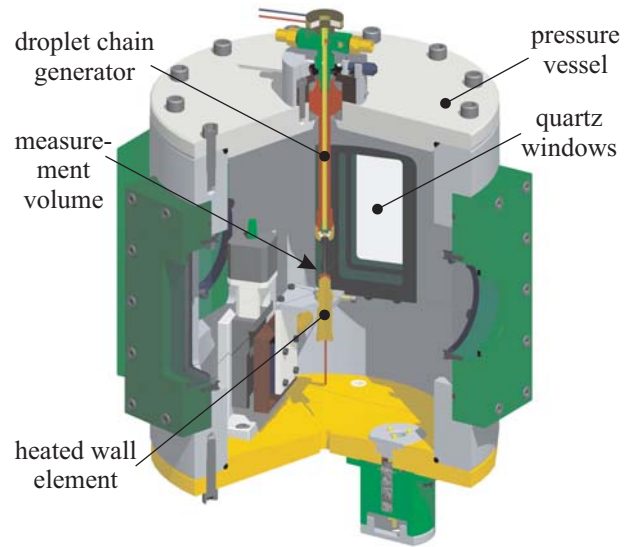

Figure 1: Schematic of the experimental setup

Wall element

The heated wall elements were fixed on a copper block that is heated by an electric heating cartridge. The surface temperature was controlled by a closed loop regulator and monitored by a thermocouple mounted directly beneath the impact location in the wall element. Temperatures can be set up to T_{wall}=412 °C, which is equivalent to a dimensionless wall temperature of $T^* = T_{wall}/T_{sat} = 1.4$ at maximum pressure.

Figure 2 shows the piston that was used in experiments by Müller et al. [4, 5] and Richter et al. [1, 2, 3] as well as other researchers of the European DWDIE project. It was chosen deliberately to give every participant the same experimental conditions with respect to surface and material properties. The wall elements were cut from this piston. The alloy is patented and available under the brands Mahle 124 or KS 1275 which is equivalent to material number 3.4032 or AlSi12CuMgNi. The physical properties are listed in table 2. The piston crown is characterized by three different regions that have different surface properties, accordingly. These surfaces were casted, rough turned and fine turned. Clearly, the physical properties of those wall elements perfectly match the properties of a real piston. A drawback is that only three grades of surface roughness are available which are furthermore in a fixed combination with surface structure.

Figure 3 shows a section for each of the three different regions in the sample piston to characterize a typical piston surface. The roughness was measured by means of a scanning electron microscope (SEM). Roughness ranges from $R_z = 14.1 \,\mu m$ for the rough turned region down to $R_z = 5.8 \,\mu m$ for the fine turned region. The roughness has different wave lengths R_w, flank angles and patterns.
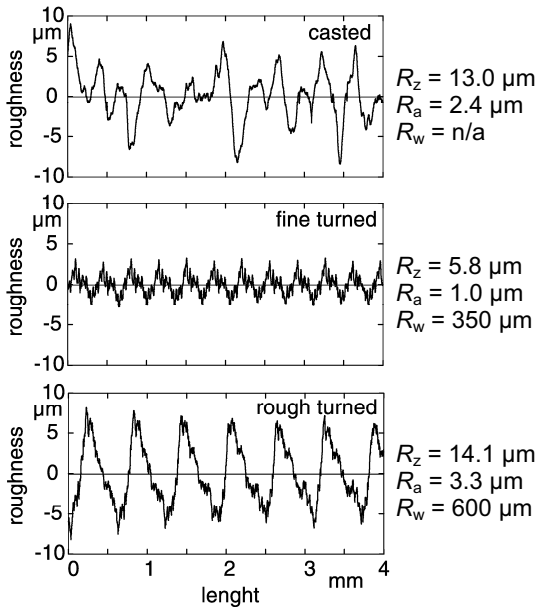

Figure 2: Piston crown with different surface qualities

Figure 3: SEM profiles of the surfaces

To characterize roughness, the roughness depth R_z and average roughness R_a, as defined in DIN/ISO, were chosen. Because R_a and R_z are independent of the distribution of the roughness elements over the surface area, additionally the roughness wavelength R_w is introduced here, which is not defined in DIN/ISO. R_w defines the lateral distance between two grooves or cones.

Various possible methods were evaluated to manufacture the surface roughness like micro milling, laser milling, systematic turning on a lathe or direct imaging onto an offset printing plate. Either the method was too time consuming, too expensive or too inflexible. Finally, two methods, sandblasting and chemical etching, were selected.

The chosen material AlMg3 has very similar physical properties compared to a typical piston alloy. As a drawback, it is hard to etch because aluminium is passivating immediately after machining and therefore is chemically inert. It was subjected to sandblasting.

Different metals and acids/bases were tested for the etching process. The etching rate had to be slow enough to stay controllable, but fast enough to be practicable. The metal had to possess physical properties similar to the piston material, and it was required that the corresponding etchant allowed handling with only moderate safety measures (with respect to toxication and chemical burning). The best compromise was CuZn37 ("brass") which is predestined for chemical etching. It is an alloy with a low electron potential that allowed using a rather weak acid. The material is more dense, but heat transfer and heat capacity per volume match very well. Table 2 shows the physical properties of the original wall element as well as the AlMg3 and CuZn37 (brass).

For etching, a number of processing steps were necessary [14]. The desired surface pattern is drawn using an automated script that is controlling a computer graphics programme. This pattern is printed with a high resolution laser printer in 5080 dpi onto an offset film. Fig. 4 shows an example that has been oversized for clarity. It has a regular structure that consists of a hexagonal array of circular roughness elements of $D_M = 1000 \,\mu m$ diameter and $R_w = 1666 \,\mu m$ pitch. The brass plate is coated with a photo resist. This resist is masked with the film, exposed to UV radiation and developed. The exposed areas are etched with sodium persulfate ($Na_2S_2O_8$). In a last step, the acid is neutralized in water and the resist is cleansed.
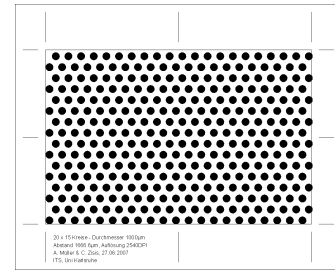

Figure 4: Etching mask with $D_M = 1000 \,\mu m$ roughness element diameter and $R_w = 1666 \,\mu m$ pitch (oversized)

Timing is critical and has to be calibrated beforehand. All other factors like temperatures, concentrations, coating thickness and radiation time are held constant. Figure 5 exemplarily shows the correlation between etching time and roughness R_z for three different masks. It can clearly be seen that for the first three minutes, etching is progressing with a constant rate. This can be explained by the scheme in Figure 6, where initially in (a) and (b) the surface is etched vertically. Later on, the resist is being undercut (c), so that truncated cones with a constant flank angle are formed. Circulation of the etchant is getting worse, so the etching rate is stagnating. The cones are getting narrower along the circumference until the resist is cut off (d). At this point, roughness is even decreasing. As can be seen in figure 5, the larger structures are less vulnerable to undercutting and hence can form deeper trenches. With the 25 µm fine structure, up to $R_z=30 \,\mu m$ roughness can be realized, whereas more than $R_z=80 \,\mu m$ are possible with the 125 µm structure.

Three examples of the etched wall elements are depicted in figure 7. In (a) the polished surface is shown. (b) and (c) are etched with a mask that has 50 µm diameter circles and $R_w = 83.3 \,\mu m$ pitch. Depth is $R_z = 13.7 \,\mu m$ and 26.7 µm, respectively.
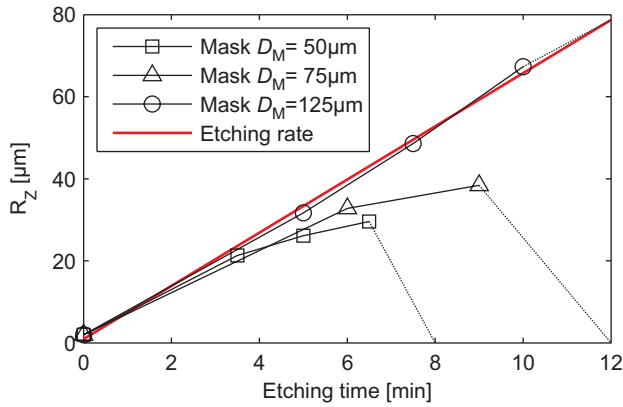
Figure 5: Calibration of the etching process

Figure 8: Calibration of the sandblasting process

Material	λ [W/(mK)]	ρ [kg/m^3]	c_p [J/(kg K)]	Hardness [Mohs]
Al	237	2700	900	2.75
AlSi12 CuMgNi	155…160	2700	900	40…160 HB
AlMg3	140…160	2660	900	45 HB
CuZn37	120	8440	377	≈3

Table 2: Material properties of different alloys at ambient temperature
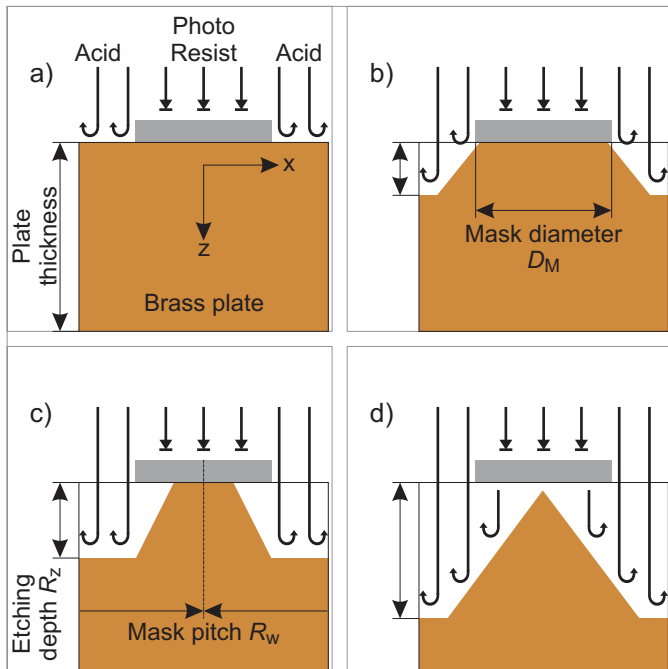
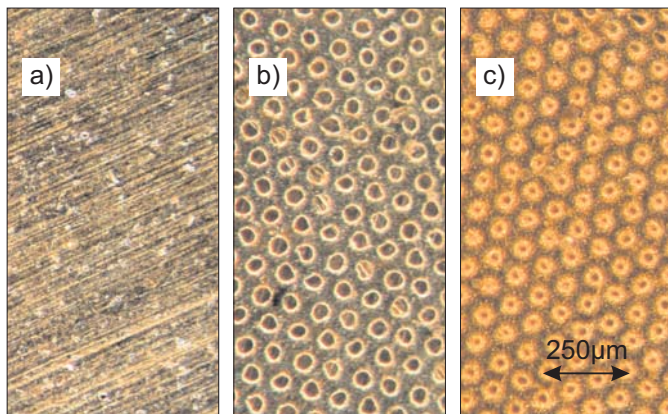

Figure 6: The series of processing steps during etching

For sandblasting, a series of material samples was processed for calibration purposes. Three different blasting abrasives were used that have different hardnesses on the Mohs scale, namely aluminium oxide (9 Mohs, coarse grain), glass beads (8 Mohs, fine grain), and sand (7 Mohs, medium grain). In addition, each abrasive was available in different grain sizes. Figure 8 shows the results of the calibration. The diagram shows roughness over sandblasting air pressure. Clearly, there is a square root dependency on the curves for each abrasive, which means that there is a correlation between kinetic energy and depth of penetration. A polished wall element has a roughness of $R_z = 2$ µm, whereas the coarse grain aluminium oxide reaches up to $R_z = 80$ µm. It is to note that the average roughness R_a scales linearly with R_z (not shown here). Furthermore, probes that yield the same roughness R_z but were processed with different grain size also differ in roughness wavelength R_w. Figure 9 exemplarily shows three surfaces that were polished to $R_z = 2$ µm (a), blasted with sand to $R_z = 13.7$ µm (b), and blasted with glass beads to $R_z = 49.9$ µm (c).

With that knowledge, two sets of 11 sandblasted and 11 etched wall elements were manufactured with different grades of roughness. The artefacts were verified by means of a Perthometer (Mahr, Concept). Although there are many common features between the etched and sandblasted wall elements like physical properties and adjustable roughness depth R_z, there are still some differences. Most notable the roughness wavelength R_w and the spatial distribution of roughness elements can be exactly controlled via etching, while it is random in the sandblasting process (Table 3).
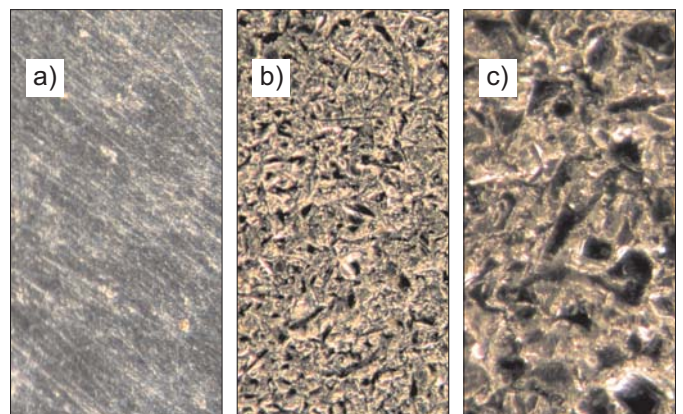

Figure 7: Exemplary microscope images of etched surfaces ($D_M = 50$ µm, $R_w = 83.3$ µm)

Figure 9: Exemplary microscope images of blasted surfaces

4

Aspect	Etching	Sandblasting
R_z	variable, but constant	variable, but random
R_a	f(R_z)	f(R_z)
R_w	arbitrary	f(R_z)
flank angle	constant	random
structure	arbitrary, e.g. regular	random

Table 3: Comparison between surface properties that can be achieved by etching or sandblasting

DIAGNOSTIC TECHNIQUE

An extended particle tracking (PTV) method was used as diagnostic technique [15, 4, 5]. It simultaneously provides the 2D position, velocity and diameter of all droplets within the depth-of-field plane. Due to the large magnification – the field of view measures only 3.6 mm × 2.9 mm – the depth-of-field is approx. 15 µm. In contrast to simplistic algorithms used in other studies, the underlying algorithm in this paper is capable to discriminate between background, wall, primary droplets, secondary droplets and the wall film.

The optical setup for the PTV is shown in Figure 2. A dual cavity Nd:YAG pulse laser provided short time high power back light illumination. The delay was adjusted according to the operating conditions between Δt=2 µs and 7 µs. The beam profile was broadened by an expansion lens and equalized in intensity by means of a diffuser disc. Due to interference effects, laser speckles generated at the diffuser would render the images useless. To overcome this phenomenon, a cuvette containing a laser dye was inserted in the optical path. It absorbed the coherent laser light and emitted incoherent light of a different wavelength. After crossing the measurement volume, the backlight was recorded by a double frame PIV camera.

RESULTS AND DISCUSSION

On heated surfaces, the different boiling regimes play an important role. In a first step, the regime change between nucleate boiling and film boiling was determined. This is done via two methods, by visualization and by monitoring the surface temperature. The different regimes can be identified of a change in droplet morphology. The second indicator is the considerably lower heat transfer for film boiling. Figure 10 shows the temperature T_{wall} for the regime change plotted over roughness depths R_z. The etched wall elements had a constant roughness wavelength of $R_w = 125$ µm. The experiment was conducted under atmospheric pressure, with a primary droplet diameter of $D_b = 64$ µm and a primary droplet velocity of $u_b = 10.9$ m/s.

It can be seen that for rather smooth surfaces with $R_z \leq 15$ µm the regime change occurs at a temperature of $T_{wall} = 160$ °C ($T^* = 1,16$). In comparison, the Mahle piston wall elements fit very well. This is in agreement with Yarin and Weiss [11], that for $R_z \ll D_b$ the effects of roughness are negligible. When using a deeper roughness with $R_z > 15$ µm, it can be recognised that the temperature for regime change is increasing nearly linearly to $T = 170$ °C for $R_z = 60.4$ µm.

This effect can be explained by means of the vapour layer between wall and isooctane film as shown in fig.ure 13. This vapour layer is formed in the film boiling regime and has a stabilizing effect. If the primary droplets have not enough momentum, the vapour layer is circumventing that the primary droplets are wetting the wall. In other words, the Leidenfrost point is a combination of surface temperature and roughness. When roughness is getting deeper, there is less lateral heat and mass transfer within the vapour layer and the layer itself is growing thicker. In the same sense, as h_v is growing, the temperature difference T_{film}-T_{wall} between film and wall is increasing. Given that the film temperature is constant for the regime change, the wall temperature T_{wall} is increasing.

Analogous to roughness depth, figure 11 shows the temperature T_{wall}, where the regime change occurs, plotted over roughness width R_w. The etched wall elements had a constant roughness depth of $R_z = 15$ µm. For the turned Mahle piston probes as well as for the etched wall element with $R_w = 125$ µm, regime change occurs at 160 °C. If structure gets finer, i.e. roughness wavelength R_w gets shorter, a higher surface temperature follows. A maximum temperature of 170 °C is reached for the finest structure of $R_w = 50$ µm.

This effect can also be explained by the vapour layer, which again acts as an insulation. If the structure gets more filigrane, the microscopic trenches and conduits allow less lateral exchange of the vapour. As a consequence, the vapour layer gets thicker and establishes a higher temperature difference between wall and film. Unfortunately, the thickness of the vapour layer can't be measured directly. However, the present test rig will be instrumented in a way that the vertical heat flux and the film temperature can be determined, thus allowing to get more information about the vapour layer.

For comparison, figure 12 shows T_{wall} at the regime change plotted over roughness depth R_z for the sandblasted wall elements. Similarly as seen before, T_{wall} increases from 160 °C for a polished surface to 180 °C for a very rough surface with Rz = 66.3 µm. The temperature difference is even higher as for the etched surface with the same roughness depth. This can be accounted to the random structure of the sandblasted surface where roughness wavelength R_w is nearly proportional to R_z, but where also capillary structures exist that support the formation of a thicker vapour layer.

Similar experiments were conducted under elevated pressure. The results are similar to the atmospheric case and hence not shown for lack of space. If the wall temperature is normalized by the saturation temperature, $T^* = T_{wall}/T_{sat}$, the regime change for the rough surfaces occurs at the same normalized temperature T^*.
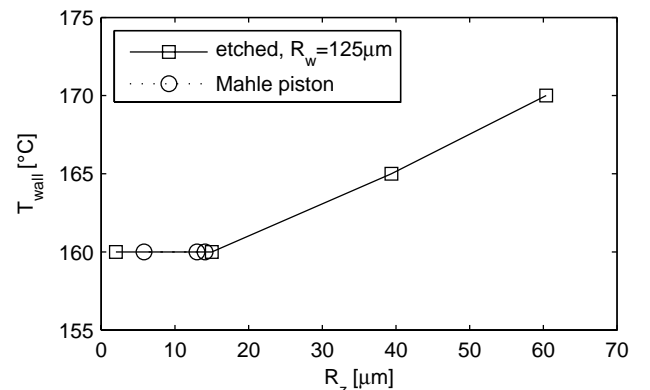

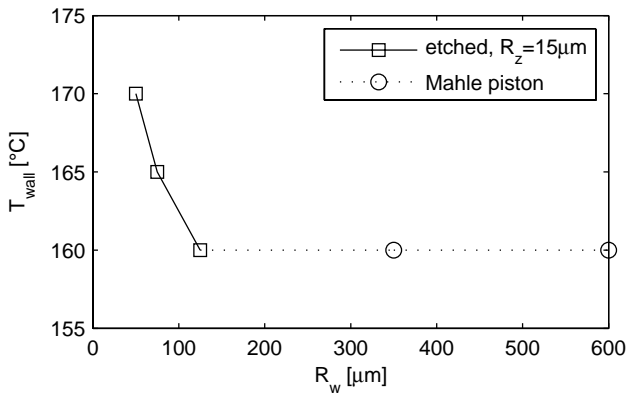Figure 10: Regime change for different roughness depths

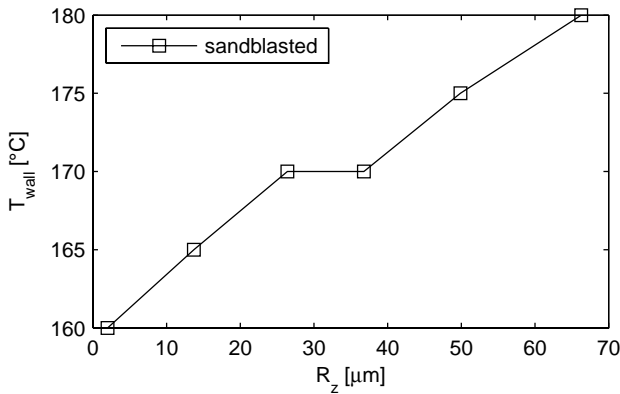Figure 11: Regime change for different roughness wavelengths

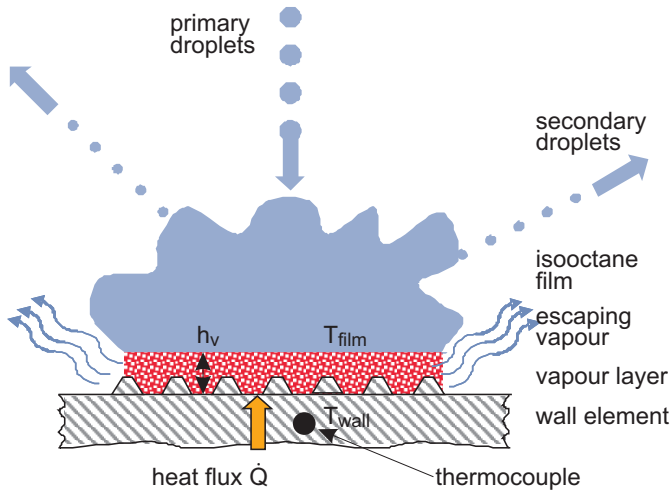Figure 12: Regime change for different sandblasted structures

Figure 13: Schema of the droplet impact on a rough surface

In a next step, particle tracking velocimetry (PTV) was applied to the droplet-wall-impact phenomenon to get a quantitative measure for the behaviour of the secondary droplets. Figure 14 shows some sample images for three different wall elements that were examined at the same operating point. The primary droplets had $u_b = 10.9$ m/s and $D_b = 64$ µm. The wall temperature was set just above the point where film boiling begins, respectively. In (a) the wall was polished. It can clearly be seen that there is a wall film and secondary droplets move rather parallel over the surface. Also, the secondary droplets are rather small and escape in every radial direction. In comparison, (b) shows a visualization for an etched wall element with a fine structure, that is $R_z = 13.7$ µm and $R_w = 50$ µm. The wall film was now less pronounced. The secondary droplets formed a spray cone with a higher elevation that consists of several streaks. Only

one streak on the left hand side was in the focal plane. This is in agreement with Mundo et al. [10], where horizontal velocity components are dissipated due to friction on the rough wall. The wall element with the coarsest structure is shown in (c) with $R_z = 60.4$ µm and $R_w = 125$ µm. Now, no wall film is visible at all. It seems to completely immerse in the structure. Mundo et al. [10] made a similar observation. Two streaks of secondary droplets are visible that have a high elevation and consist of droplets that are of similar size as the primary droplets.

For every operating point, a series of 300 images were taken. Exemplary results of the PTV analysis are shown in Figure 15, which corresponds to case (a) in Figure 14. The top diagram shows a vector plot of mean particle velocity for both magnitude and direction per interrogation spot. It can be seen that the secondary droplets move nearly horizontally and the spray cone spreads symmetrical. The colour in the background indicates the mean droplet diameter per interrogation spot. To get more condensed numbers, all secondary droplets in all images of a series are plotted as a velocity spectrum (middle) and a diameter spectrum (bottom). In this case, the arithmetic mean velocity is $u_a = 2.9$ m/s and the arithmetic mean diameter $D_a = 33$ µm.
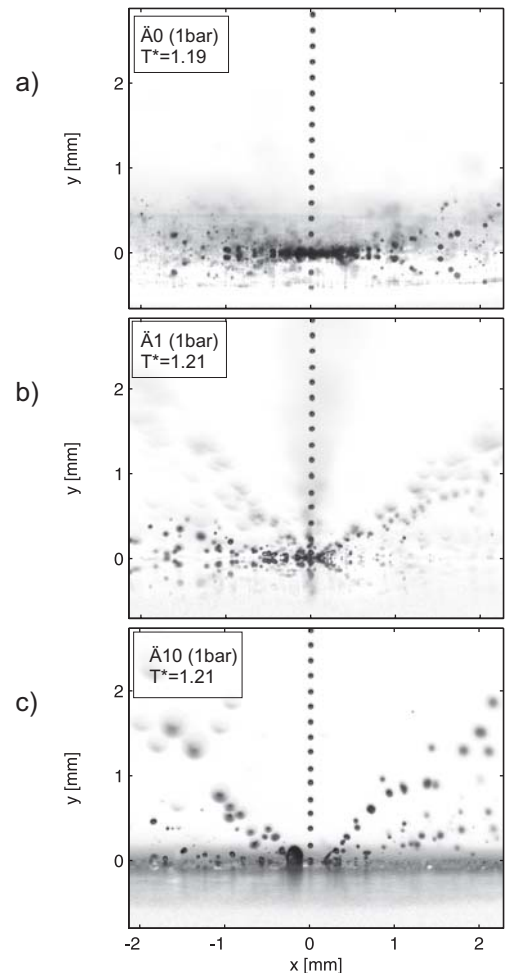

Figure 14: Droplet impact on a rough surface

Table 4 summarizes the effect anticipated in the visualizations. For the polished surface, a nominal secondary droplet diameter of $D_a = 33$ µm and velocity of $u_a = 2.9$ m/s is obtained. As soon as there are narrow and/or deep structures on the surface, a thicker vapour layer is evolving. This leads to the fact that for the narrowest structure examined ($R_z = 13.7$ µm / $R_w = 50$ µm), droplet diameter increases to

41 µm and velocity decreases to u_a = 2.2 m/s. For the deepest structure examined (R_z = 60.4 µm / R_w = 125 µm), the secondary droplets are approximately as big as the primary droplets and reducing speed to u_a = 1.9 m/s. In other words, it can be asserted that the vapour layer is damping the impulse of the impact and hindering atomization.

Rz	Rw	D_b	u_b	T^*	D_a	u_a
[µm]	[µm]	[µm]	[m/s]	[1]	[µm]	[m/s]
2.0	-	64	10.9	1.19	33	2.9
13.7	50	64	10.9	1.21	41	2.2
60.4	125	63	10.7	1.21	60	1.9

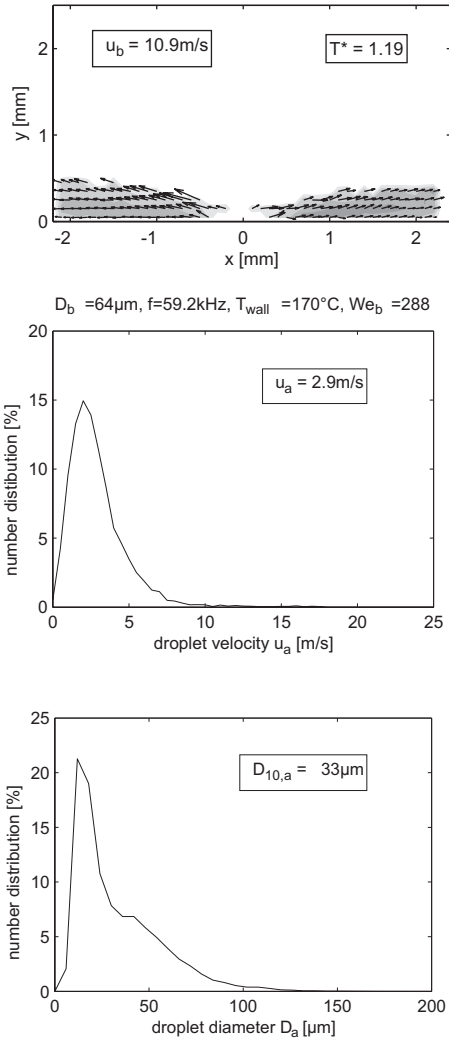Table 4: Secondary droplet characteristics after impact on a rough surface

Figure 15: Analysis example for one surface with secondary droplet velocity vectors (top), velocity spectrum (middle) and diameter spectrum (bottom)

SUMMARY

In the present work, the impact of surface structure on droplet wall interaction has been investigated. Two procedures were developed to generate surfaces with a well defined roughness, an etching and a sandblasting process are used. Two series of wall elements with different grades of surface roughness were manufactured. It was found that roughness has an influence on droplet-wall-interaction on heated surfaces. An increased roughness depth R_z as well as a short roughness wavelength R_w support the formation of a thicker vapour layer between surface and fuel film which is insulating the wall surface thermally. Furthermore it is damping the primary droplet impact. As a consequence, the wall gets hotter, the secondary droplets bigger and slower. This has negative effects on atomization and component temperatures.

For more evidence, further experiments have to be done. Especially heat transfer from the wall element to the fuel has to be measured. Modelling of the heat and mass transfer is necessary. Furthermore, it was found that the surface pattern has an influence, e.g. where the primary droplets hit a roughness element. This adds an additional complexity to further experiments.

ACKNOWLEDGMENT

NOMENCLATURE

Symbol	Quantity	SI Unit
c_D	discharge coefficient	1
c_p	specific heat capacity	J/(kg K)
d	orifice diameter	m
D	diameter	m
f	excitation frequency	1/s
h_v	thickness of vapour layer	m
$\dot{m}$	mass flow rate	kg/s
p	pressure	Pa
R_a	roughness, arith. Average	m
R_t	roughness, min./max.	m
R_w	roughness, wavelength	m
R_z	roughness, min./max. over 5 traces	m
S_t	roughness number (Mundo)	1
T	temperature	°C
u	droplet velocity	m/s
$\dot{Q}$	heat flux	W/m²
λ	thermal conductivity	W/(m K)
μ	dynamic viscosity	Pa s
ρ	density	kg/m³
σ	surface tension	N/m

Index	Meaning
a	droplet after impact
b	droplet before impact
M	mask
V	vapour

REFERENCES

[1] B. Richter, K. Dullenkopf and S. Wittig, Wall impact of single droplets under conditions of DISI-Engines, *9th Int. Conf on Liquid Atomization and Spray Systems*, Sorrento, Italy, 2003

[2] B. Richter, K. Dullenkopf and H.-J. Bauer, Investigation of Secondary Droplet Characteristics Produced During Wall Impact, *12th Int. Symp. Applications of Laser Techniques to Fluid Mechanics*, Lisbon, Portugal, 2004

[3] B. Richter, K. Dullenkopf and H.-J. Bauer, Investigation of Secondary Droplet Characteristics Produced by an Isooctane Drop Chain Impact Onto a Heated Piston Surface, *Experiments in Fluids*, vol. 39, pp. 351-363, 2005

[4] A. Müller, F. Schumann, K. Dullenkopf and H.-J. Bauer, Analysis of Droplet Wall Interaction using Advanced Image Processing Techniques, *Proc. 21st ILASS Europe*, Muğla, Turkey, 2007

[5] A. Müller, K. Dullenkopf and H.-J. Bauer, Application of an Extended Particle Tracking Method to Analyze Droplet Wall Interaction, *14th Int. Symp. on Applications of Laser Techniques to Fluid Mechanics*, Lisbon, Portugal, 2008

[6] I.V. Roisman, K. Horvat and C. Tropea, Spray impact: Rim transverse instability initiating fingering and splash, and description of a secondary spray, *Physics of Fluids*, vol. 18, 2006

[7] G.E. Cossali, M. Marengo and M. Santini, Single-Drop Empirical Models for Spray Impact on Solid Walls - A Review, *Atomization and Sprays*, vol. 15, pp. 699-736, 2005

[8] C. Bai and A.D. Gosman, Development of Methodology for Spray Impingement Simulation, SAE Technical Paper No. 950283, 1995

[9] C. D. Stow and M. G. Hadfield, An Experimental Investigation of Fluid Flow Resulting from the Impact of a Water Drop with an Unyielding Dry Surface, *Proc. Royal Society of London. Series A, Mathematical and Physical Sciences*, vol. 373, no. 1755, pp. 419-441, 1981

[10] C. Mundo, M. Sommerfeld and C. Tropea, Droplet-Wall Collisions: Experimental Studies of the Deformation and Breakup Process, *Int. J. Multiphase Flow*, vol. 21, no. 2, pp. 151-173, 1995

[11] A.L. Yarin and D.A. Weiss, Impact of drops on solid surfaces: self-similar capillary waves, and splashing as a new type of kinematic discontinuity, *J. Fluid Mech*, vol. 283, pp 141-173, 1995

[12] K. Anders, N. Roth and A. Frohn, Operation Characteristics of Vibrating-Orifice Generators as a Calibration Standard for Sizing Methods and for the Study of Basic Phenomena, *Proc. 2nd Int. Congr. on Optical Particle Sizing*, 1990

[13] J.W.S.L. Rayleigh, The Theory of Sound, Macmillan, London, 1877

[14] M. Stripf, A. Schulz and S. Wittig, Surface Roughness Effects on External Heat Transfer of a HP Turbine Vane, *J. of Turbomachinery*, vol. 127, pp. 200-208, 2005

[15] A. Müller, R. Koch, H.-J. Bauer, M. Hehle and O. Schäfer, Performance of Prefilming Airblast Atomizers in Unsteady Flow Conditions, *ASME Paper GT2006-90432*, Barcelona, Spain, 2006